GEOPHYSICS, VOL. 71, NO. 6 (NOVEMBER-DECEMBER 2006); P. N47–N56, 8 FIGS., 3 TABLES.
10.1190/1.2353803

Theory of vibratory mobilization on nonwetting fluids entrapped in pore constrictions

Igor A. Beresnev[1]

ABSTRACT

Quantitative dynamics of a nonwetting ganglion of residual oil entrapped in a pore constriction and subjected to vibrations of the pore wall can be approximated by the equation of motion of an oscillator moving under the effect of the external pressure gradient, inertial oscillatory force, and restoring capillary force. The solution of the equation provides the conditions under which the droplet experiences forced oscillations without being mobilized or is liberated from its entrapped configuration if the acceleration of the wall exceeds an unplugging value. This solution provides a quantitative tool for estimating the parameters of vibratory fields needed to liberate entrapped, nonwetting fluids. For typical pore sizes encountered in reservoir rock, wall accelerations must exceed at least several m/s^2 and even much higher levels to mobilize the droplets of oil; however, in the populations of ganglia entrapped in natural porous environments, many may reside very near their mobilization thresholds and may be mobilized by extremely low accelerations as well. For given acceleration, lower seismic frequencies are more efficient in liberating the ganglia.

INTRODUCTION: THE PROBLEM

Mobilization of residual oil by elastic waves and vibrations has long been considered a possible method of enhanced petroleum recovery (Beresnev and Johnson, 1994; Nikolaevskiy et al., 1996; Poesio et al., 2002; Roberts et al., 2001, Roberts et al., 2003; Roberts, 2005). Over the past few years, a number of studies have been devoted to a theoretical justification of the method at the pore level. They sought an explicit description of the pore-scale mechanism by which the vibrations mobilized the entrapped nonwetting fluids, which could then be used to predict the results of field applications. On the basis of the Poiseuille flow approximation, Hilpert et al. (2000) calculated the frequencies of pulsing pressure in an axisymmetric channel with a sinusoidal profile that maximized the volume of the displaced nonwetting phase. Although no explicit mobilization criteria were established, it was proposed that the entrapped-blob oscillations at these resonance frequencies could lead to blob liberation. Graham and Higdon (2000) and Beresnev et al. (2005) developed a complete computational-fluid-dynamics (CFD) simulation of the mobilization of spherical droplets in constricted cylindrical channels. Iassonov and Beresnev (2003) formulated a theory of vibratory mobilization for the scenarios in which the fluid exhibited a yield-stress behavior caused by either its rheology or the postulated fluid pinning on the wall, albeit without considering a specific pinning mechanism. In a more recent study conducted by Iassonov and Beresnev (manuscript in review, 2006), the mobilization theory in sinusoidally constricted channels was formulated in the approximation of laminar Poiseuille flow, which again had to be justified through a complete CFD simulation for every channel profile used.

Despite the significant progress achieved in understanding the conditions for oil-blob mobilization by elastic waves and vibrations, a physical theory that could readily be used to calculate the mobilization conditions for given geometric parameters of the channel, frequency, and amplitude of the vibratory field is still missing. The CFD models described still require the use of supercomputers, even for the simplest geometries, and do not offer much physical insight. A predictive model that could provide a transparent physical analysis of the mobilization process is needed to advance its practical applications. The theory developed in this paper fills this gap.

The article proceeds as follows. We start with a brief outline of the capillary mechanism of the vibratory mobilization of entrapped nonwetting fluids. An equation of motion incorporating the elements of this mechanism is then derived, followed by a quantitative analysis of the mobilization phenomenon for typical scenarios based on the solutions of this equation. Conclusions are provided with the main inferences from the numerical analysis. Appendices A and C are devoted to the verification of the assumptions made to simplify the numerical analysis, and Appendix B contains an exact calculation of

Manuscript received by the Editor January 26, 2006; revised manuscript received May 10, 2006; published online October 23, 2006.
[1]Iowa State University, Department of Geological and Atmospheric Sciences, 253 Science I, Ames, Iowa 50011. E-mail: beresnev@iastate.edu.

the center of mass of a droplet in a constricted channel, used in formulating the governing equation.

PHYSICAL MECHANISM OF THE VIBRATORY MOBILIZATION OF ENTRAPPED NONWETTING GANGLIA

To set the stage for the description of the mobilization phenomenon, we first review the capillary mechanism of the mobilization as illuminated by Graham and Higdon (2000) and Beresnev et al. (2005).

Capillary forces cause the entrapment of ganglia of a nonwetting fluid in pore constrictions. Let us assume, for simplicity, spherical menisci and complete nonwetting. When the leading meniscus of the oil blob is in the constriction, a capillary-pressure imbalance builds up inside the ganglion according to the Laplace equation,

$$\Delta P_{\text{cap}} = 2\sigma\left(\frac{1}{R_2} - \frac{1}{R_1}\right), \tag{1}$$

where R_2 and R_1 are the radii of the downstream and the upstream menisci, respectively, and σ is the oil/water interfacial tension. This internal pressure difference opposes the external pressure drop across the length of the ganglion caused by the external pressure gradient; when these two equalize, the ganglion is entrapped (Figure 1 of Beresnev et al., 2005). The external gradient needs to exceed a certain unplugging threshold ∇P_0 to move the ganglion through the capillary barrier.

The conditions for the entrapment and mobilization can be graphically illustrated on the diagram in Figure 1 (straight line), which shows the oil flow rate as a function of applied external force, where ∇P_s is the static external gradient attempting to drive the ganglion through the constriction (Beresnev et al., 2005). The flow is plugged, and the oil resides in static equilibrium as long as $|\nabla P_s| < |\nabla P_0|$ (the no-flow zone), above which it resumes at a normal Darcy rate (the flow zone). In the frame of reference of the wall, the application of longitudinal vibrations of the wall is equivalent, for a cylindrical channel, to the addition of an inertial body force acting on the fluid, $F_{osc}(t) = -\rho_f a(t)$, where ρ_f is the density of the fluid and $a(t)$ is the acceleration of the wall (Biot, 1956, equation 2.4). Here, without the loss of generality, we consider the component of the wall motion along the pore axis. Because the length of an oil ganglion is much smaller than the seismic wavelength, the body force can be considered constant. This oscillatory force is added to the external gradient as illustrated by its time history plotted vertically around ∇P_s in Figure 1. If it is sufficiently strong to satisfy the condition

$$|\nabla P_s| + |F_{\text{osc}}| > |\nabla P_0|, \tag{2}$$

then over the period of time when this condition holds, the ganglion is unplugged and moves forward beyond the neck of the constriction. The radius of the leading meniscus then starts to increase progressively, which leads to the decrease in the resisting capillary force. As a result, the ganglion accelerates upon exiting the constriction, experiencing what is often called a Haines jump (e. g., Melrose and Brandner, 1974). This leads to its mobilization. The condition expressed by inequality 2 can be referred to as the static mobilization criterion. It assumes that the ganglion has enough time over one period of vibration to be brought to the neck of the constriction, which can only happen if the period is long enough. Clearly, if the frequency is sufficiently high, this criterion breaks down; above a certain critical frequency, the ganglion is no longer liberated with the vibration amplitude following from the static criterion. The ganglion can nevertheless still be mobilized if the amplitude increases to compensate for the lack of time to reach the neck; the mobilizing amplitude can thus be expected to increase with the frequency above the critical-frequency value. The critical frequency can be obtained from the equation of motion of the ganglion. The decrease in the mobilizing effect of vibrations with increasing frequency, predicted by this mechanism, was experimentally demonstrated by Li et al. (2005).

The dynamics of the ganglion's motion and liberation from the entrapped configuration for an arbitrary amplitude and frequency can be obtained through quantitative modeling of the mechanism shown in Figure 1. In the next section, we proceed to the formal statement of this problem.

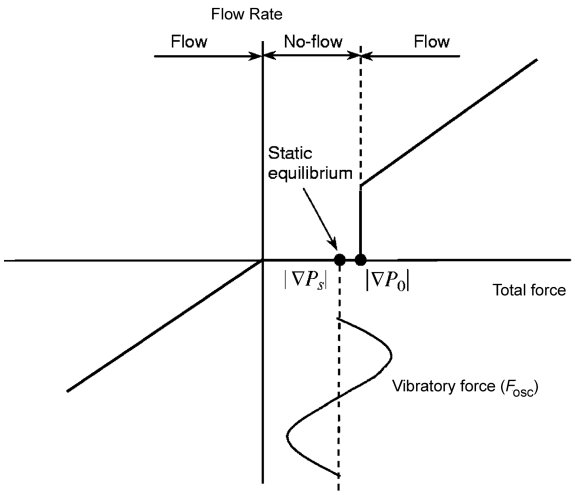

Figure 1. The mechanism of oil-ganglion liberation under the combined effect of external pressure gradient and oscillatory force.

MODEL FORMULATION

Problem geometry

We will consider an axisymmetric, periodically constricted sinusoidal channel, whose radius varies with the axial coordinate z as

$$r(z) = r_{\max}\left[1 + \frac{1}{2}\left(\frac{r_{\min}}{r_{\max}} - 1\right)\left(1 + \cos\pi\frac{z}{L}\right)\right], \tag{3}$$

where $r_{\min}$ and $r_{\max}$ are the minimum and the maximum radii and $2L$ is the spatial period. The geometry of the problem is illustrated in Figure 2, where the sinusoidal channel and the ganglion in it are

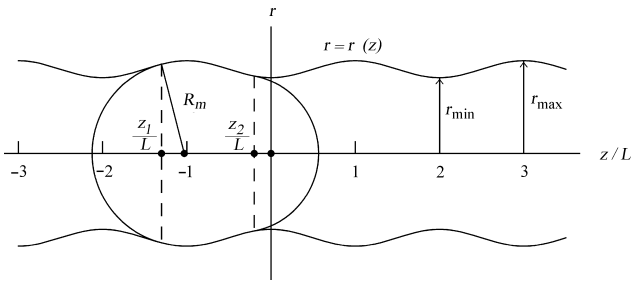

Figure 2. Geometry of the problem.

shown; z_1 and z_2 are the coordinates of the three-phase upstream and downstream contact lines, respectively, and R_m is the radius of the spherical menisci. The ganglion's motion under the external gradient is from left to right. A zero contact angle (complete nonwetting by oil) is again assumed. The meniscus radius is then related to the coordinate of the contact line as

$$R_m(z_{1,2}) = r(z_{1,2})\sqrt{1 + r'^2(z_{1,2})}, \tag{4}$$

where $r'(z)$ is the derivative, $R_m(z_1)$ is the radius of the trailing meniscus and $R_m(z_2)$ is the radius of the leading meniscus.

A limitation of this representation of the menisci as continuous spherical surfaces is that they may not intersect the walls of the channel. This is equivalent to the requirement that the menisci radius of curvature always be smaller than that of the wall profile. The radius of curvature of the wall is $R_{\text{curv}} = (1 + r'^2)^{3/2}/|r''|$ (e.g., Harris and Stocker, 1998, p. 520). For a sinusoidal function, the minimum radius of curvature occurs at its crests, where, from equations 3 and 4, the meniscus radius is $r_{\max}$. Calculating R_{curv} at the crests of the profile described by equation 3 and requiring that it be greater than $r_{\max}$, leads us to the no-intersection condition

$$\frac{2L^2}{\pi^2 r_{\max}(r_{\max} - r_{\min})} > 1, \tag{5}$$

which restricts the channel geometries that can be used in our model.

Equation of motion

A nonwetting oil ganglion can reasonably be assumed to slide along the wetting film of water on the pore wall as a moving mass with little interaction and, therefore, little friction, at least near the static equilibrium before it is mobilized. For comparable densities of oil and water, the oscillatory body force $F_{\text{osc}}(t) = -\rho_f a(t)$ applied to both fluids is approximately the same; the oil motion is restricted by the resisting capillary force and the water motion by the viscosity; the relative motion of oil and water can in the first approximation be neglected (a more quantitative justification of this assumption is provided in a later section). The behavior of the ganglion can then be reasonably approximated as that of a frictionless body driven by the balance of forces acting upon it, which include the external gradient, the capillary force resisting it, and the oscillatory body force induced by the vibrations. The resultant force is applied to the center of mass of the body. Such a representation, of course, will be only valid prior to the leading meniscus crossing the neck of the constriction, after which the ganglion will start to accelerate infinitely because the restricting capillary force will no longer be present. The behavior of the ganglion in this configuration is nevertheless of little interest to us, because we only seek the conditions leading to the mobilization.

A similar approach was taken by Averbakh et al. (2000) to study the mobilization dynamics of a droplet of wetting fluid in a straight channel whose entrapment was caused by the contact-angle hysteresis, that is, a different physical phenomenon.

Writing the second Newton's law for the balance of forces acting upon the ganglion, we obtain the equation of motion in the form

$$\rho_o V_g \frac{d^2 z_c}{dt^2} = -\nabla P_s V_g - \rho_o a(t) V_g + \frac{2\sigma V_g}{z_2 - z_1}\left[\frac{1}{R_m(z_1)} - \frac{1}{R_m(z_2)}\right], \tag{6}$$

where z_c is the coordinate of the center of mass, ρ_o is the density of oil, and V_g is the ganglion's volume. Here, the last term on the right-hand side is the capillary force, obtained from the capillary-pressure difference, as in equation 1, by switching to its gradient. The signs of all forces have been taken into account, considering that the force is positive if it acts to the right. The volume cancels out in equation 6, leaving the balance of pure body forces.

With the use of equation 4 for the menisci radii, equation 6 transforms to

$$\rho_o \frac{d^2 z_c}{dt^2} = -\nabla P_s - \rho_o a(t) + \frac{2\sigma}{z_2 - z_1}\left[\frac{1}{r(z_1)\sqrt{1 + r'^2(z_1)}} - \frac{1}{r(z_2)\sqrt{1 + r'^2(z_2)}}\right]. \tag{7}$$

Strictly speaking, the representation $-\rho_o a(t)$ that we use for the oscillatory body force is valid for a cylindrical channel only; in such channels, the z-derivatives of the fluid velocity vanish. We discuss the validity of this assumption for a constricted channel in Appendix A.

The exact coordinate of the center of mass of the ganglion z_c is a complicated irrational function of z_1, z_2, and the ganglion's volume V_g: $z_c = z_c\,(z_1, z_2, V_g)$, which is derived in Appendix B, equations B-1–B-8. This function should be substituted into equation 7, resulting in a differential equation for z_1, z_2, and their time derivatives. This equation then should be solved in conjunction with the equation $V_g = V_g(z_1, z_2)$, where V_g is a given fixed volume, which also is a complicated irrational function (equations B-2 and B-6–B-8). Even for the simple geometry used, to solve such a system of two equations, in which functions z_1 and z_2 and their derivatives are only implicitly defined, would be a formidable task. Simplifications must be sought.

Let us approximate the center of mass by $z_c = (z_1 + z_2)/2$, which places it in the middle of the ganglion, and assume that the ganglion is of approximately constant length l, $z_2 = z_1 + l$. These approximations are, of course, better the smaller the difference between $r_{\max}$ and $r_{\min}$ (the small-slope approximation). Because the exact values of z_c and l are known, we can always estimate how much error we commit. Appendix C provides the worst-scenario-case calculation of the error in this approximation.

With these substitutions for z_c and z_2, equation 7, normalized by L, becomes

$$\frac{d^2(z_1/L)}{dt^2} - \frac{2\sigma}{\rho_o L l}\left[\frac{1}{r(z_1)\sqrt{1 + r'^2(z_1)}} - \frac{1}{r(z_1 + l)\sqrt{1 + r'^2(z_1 + l)}}\right] + \frac{a(t)}{L} + \frac{\nabla P_s}{\rho_o L} = 0, \tag{8}$$

which describes the position of the ganglion (its left contact line) driven by the forces acting upon it.

Note that, although equation 8 is valid for any frequency of vibration, a realistic viscous fluid, whose behavior it approximates, always has a finite response time to dynamic forcing. This characteristic time scale is typically estimated from the problem of a startup flow in response to a step force. For a cylindrical channel, the fluid flow is fully developed over a time scale of

$$\tau = \frac{\rho_f r^2}{\mu}, \quad (9)$$

where r is the radius of the channel and μ is the fluid viscosity (Johnson, 1998, p. 9-11). Consequently, if the period of vibration exceeds τ,

$$T > \tau, \quad (10)$$

the fluid is allowed a sufficient time to respond, although, at shorter periods, the vibrations are inefficient in inducing the flow. The upper limit of the frequencies to be used in the vibratory stimulation of oil reservoirs is thus on the order of $1/\tau$. Our subsequent analysis will consider the frequencies lower than this upper bound. The time scale τ can be calculated from the typical viscosities of the fluids of interest. If the condition expressed by inequality 10 is satisfied, the process, itself, of the ganglion's deformation can be neglected because it can be considered instant.

RESULTS

Equation 8 has no known analytical solutions, despite the simple geometry of the problem. It was solved numerically to the precision of sixteen decimal digits. In all simulations, the following characteristic fixed values of the problem parameters were used: $L = 10^{-2}$ m, $\sigma = 0.040$ N/m, $\rho_o = 10^3$ kg/m^3; the other parameters were varied as described. The ganglion with the length $l = 0.6\ L$ was placed between values of $z/L = -1$ and 0 in Figure 2. The static initial condition $z_1/L = \text{const}$ at $t = 0$ was used, meaning that the ganglion was at rest in equilibrium between the external gradient and the resisting capillary force (the entrapped configuration). The second initial condition was zero velocity, $d(z_1/L)/dt = 0$ at $t = 0$. The sinusoidal vibration of the wall $a(t) = a_0 \sin 2\pi ft$ was turned on at $t = 0$, where a_0 is the acceleration amplitude, and f is the frequency. All simulations were run to 20 periods of vibrations.

In the following, we consider three typical combinations of r_{max} and r_{min}, representative of the range of values that can be encountered in reservoir rock. To illustrate a variety of scenarios, we consider two extreme cases of both a narrow ($r_{max} = 10^{-4}$ m, $r_{min} = 10^{-5}$ m) and a wide($r_{max} = 10^{-3}$ m, $r_{min} = 10^{-4}$ m) pore, in both of which $r_{max}/r_{min} = 10$. In addition, we consider a smooth pore ($r_{max} = 10^{-3}$ m, $r_{min} = 5 \times 10^{-4}$ m) in which $r_{max}/r_{min} = 2$. All the geometries satisfy the condition expressed by formula 5.

The narrow pore ($r_{max} = 10^{-4}$ m, $r_{min} = 10^{-5}$ m)

Here, it is instructive to analyze two cases in which (1) the static gradient ∇P_s is close to the unplugging threshold ∇P_0, and (2) ∇P_s is far from ∇P_0.

Case 1

According to equation 1, the capillary-pressure difference across the length of the ganglion is $2\sigma[1/R_m(z_1 + l) - 1/R_m(z_1)]$; for $r_{max} = 10^{-4}$ m and $r_{min} = 10^{-5}$ m, its maximum value is about 6846.1 Pa. This gives the unplugging-threshold body force $|\nabla P_0|$ of 6846.1 Pa/$(0.6 \times 10^{-2}$ m) $\approx 1.141 \times 10^6$ N/m^3. According to the idea of Case 1, we set the static gradient close to this value, $|\nabla P_s| = 1.11 \times 10^6$ N/m^3. From the criterion expressed by formula 2, we then have the following condition for the mobilization: $\rho_o a_o + 1.11 \times 10^6$ N/m$^3 > 1.141 \times 10^6$ N/m^3, from which $a_0 \approx 31$ m/s^2. This is the predicted acceleration amplitude that will mobilize the ganglion from its entrapped position.

The ganglion's equilibrium configuration for $|\nabla P_s| = 1.11 \times 10^6$ N/m^3 can be found by equating the capillary-pressure difference to the external pressure drop across the length of the ganglion, $2\sigma[1/R_m(z_1 + l) - 1/R_m(z_1)] = |\nabla P_s| l$. This algebraic equation was solved numerically to find its root z_1/L in the interval of z/L from -1 to -0.6, to yield $z_1/L \approx -0.6389$. Because the length of the ganglion $l/L = 0.6$, the right contact line is at $z_2/L \approx -0.0389$, or close to the neck of the constriction. The value of the static gradient, the entrapped configuration, and the predicted mobilizing acceleration are respectively summarized in the first three columns of Table 1.

For a characteristic fluid viscosity of 10^{-3} Pa.s, the time scale of the ganglion's response to vibrations is given by equation 9, $\tau = 10^3$ kg/m$^3 \times (10^{-4}$ m$)^2/10^{-3}$ Pa.s $= 10^{-2}$ s. This, according to equation 10, limits the frequencies of consideration for $r_{max} = 10^{-4}$ m to lower than approximately 100 Hz. Above this frequency, the vibratory action will have little effect on the fluid.

Table 1. Mobilization parameters in the narrow ($r_{max} = 10^{-4}$ m, $r_{min} = 10^{-5}$ m) pore. The capillary-threshold body force is 1.141×10^6 N/m^3, $\tau = 10^{-2}$ s.

External gradient $\lvert\nabla P_s\rvert$ (N/m^3)	Initial condition of ganglion at rest $z_1/L(t = 0)$	Mobilizing acceleration a_0 predicted from the static criterion (m/s^2)	Computed mobilizing acceleration a_0 (m/s^2)					Frequency of breakdown in the static criterion (Hz)
			0.01 Hz	0.1 Hz	1 Hz	10 Hz	100 Hz	
1.11×10^6	−0.6389	31	Between 31–32	Between 31–32	Between 30–31 (mobilized after 2 periods)	Between 27–28 (mobilized after 3 periods)	Between 32–33 (mobilized after 8 periods)	≈100
0.55×10^6	−0.8070	591	Between 591–592	Between 590–591 (mobilized after 2 periods)	Between 589–590 (mobilized after 11 periods)	Between 449–450 (mobilized after 18 periods)	Between 231–232 (mobilized after 14 periods)	≈200

In columns 4-8, Table 1 lists the amplitudes of the mobilizing acceleration that were obtained from the numerical solution of governing equation 8; these can be compared to the predicted value. The computations were carried out for the vibration frequencies of 0.01, 0.1, 1, 10, and 100 Hz. At each frequency, a_0 was increased sequentially until the mobilizing amplitude was found; its bracketed values for Case 1 are in the first row of Table 1. The ganglion was considered mobilized if it started to accelerate out of the constriction within the 20-period computation time.

Figure 3 shows the results of such computation for $f = 10$ Hz and $a_0 = 28$ m/s^2. This example shows the forced oscillations of the ganglion around its entrapped position with the driving period of 0.1 s; however, shorter-period oscillations are also clearly observed. These are the natural (free) oscillations of the droplet. The droplet confined in the constriction by the restoring forces acting both from the left (the external gradient) and from the right (the resisting capillary force) is an oscillator, having its own natural frequency. Once disturbed from the equilibrium, the droplet experiences both forced and free oscillations seen in Figure 3. Because of the nonlinear character of equation 8, it was not possible to find an analytical expression for the natural frequency; its value will clearly depend on the magnitude of the restoring force, that is, both the external gradient and the pore geometry, and will be highly variable. For the scenarios considered in this article, it ranges from ~ 1 to 100 Hz (cf. Figure 3).

The results in Table 1 show close correspondence between the predicted mobilizing acceleration and its value found from the numerical solution, for all frequencies. If the ganglion is not mobile after the first period of vibrations, the period at which it is mobilized is provided in parentheses in Table 1. Generally, the higher the frequency, the more periods are necessary for the mobilization to occur. This tendency is explained by the superposition of forced and free oscillations of the ganglion. Their interference causes fluctuations in the current droplet position, pushing it closer or further away from the neck of the constriction. Because of these fluctuations that are difficult to quantitatively predict, the mobilization may not occur until the period in which both types of oscillations add up in such a way as to push the ganglion sufficiently far into the neck; for example, as in period 3 (around 0.3 s) in Figure 3. When the forcing period is long compared to the free period, there is a high probability that such a constructive interference occurs during the first vibratory cycle; however, when the forcing period becomes smaller, such conditions may not materialize until subsequent cycles. For example, at the vibration frequency of 100 Hz, the ganglion is not mobilized until the eighth cycle of vibrations (Table 1).

The mobilization moment is clearly indicated in the simulations as the time of the beginning of a precipitous withdrawal of the ganglion from the constriction (approximately 0.3 s in Figure 3). Such divergent solutions, of course, are of no interest because our goal is to track the ganglion only until it has been mobilized.

The mobilizing amplitude calculated from the static criterion in equation 2 breaks down if the frequency is high enough that this amplitude becomes insufficient to move the ganglion to the neck of the constriction. Above this critical frequency, the mobilizing amplitude must increase. The critical frequency can be estimated from the time it takes for the droplet to move from its entrapped to mobilized configuration for a step increase in external force from ∇P_s to ∇P_0. Then, if the vibratory period is longer than the critical period, the ganglion will experience, approximately, a sufficient forcing near the maxima of F_{osc} to be transported to the neck. For Case 1, it was checked numerically that the ganglion was fully mobile for $|\nabla P_0| = 1.15 \times 10^6$ N/m^3. Subject to a step increase in external force from $|\nabla P_s| = 1.11 \times 10^6$ N/m^3 to $|\nabla P_0| = 1.15 \times 10^6$ N/m^3, it took approximately 0.01 s to become mobilized. This estimates the frequency of the breakdown in the static criterion to be on the order of 100 Hz; this value is listed in the last column of Table 1. Note that all frequencies considered in Case 1 turned out to be below this critical value, which explains the independence of the mobilizing amplitude on the frequency of vibrations. The case when the critical frequency is sufficiently low to show its effect on the mobilizing acceleration is considered in a later section.

Case 2

For Case 2, the static gradient is set away from the unplugging threshold, $|\nabla P_s| = 0.55 \times 10^6$ N/m^3 (approximately half of its value for Case 1). From the calculations similar to those shown for Case 1, we obtain the predicted mobilizing acceleration of ~ 591 m/s^2, and the entrapped position $z_1/L \approx -0.8070$. The ganglion's right contact line is, therefore, at $z_2/L \approx -0.2070$, or far from the neck. Table 1 (second row) lists all the Case 2 parameter values and the results of numerical simulation in the same format as for Case 1.

Figure 4 is an example of the ganglion's behavior at $f = 0.01$ Hz and $a_0 = 591$ m/s^2 (just below the mobilizing value of 592 m/s^2). This example illustrates the forced oscillations of the blob around its equilibrium, with hikes to very near the level of $z_1/L = -0.6$, and demonstrates the need for the latter's exceedance. Once pushed slightly past this level, which happens at $a_0 = 592$ m/s^2, the ganglion becomes mobilized.

From Table 1, the mobilizing acceleration predicted from the static criterion and that obtained from the numerical solution agree well up to the frequency of 10 Hz, at which the actual acceleration drops to between 449 to 450 m/s^2, and even further to 231 to 232 m/s^2 at 100 Hz. A significant increase in the total number of periods elapsed before the mobilization took place can also be noticed toward these higher frequencies. Both the drop in the acceleration and the in-

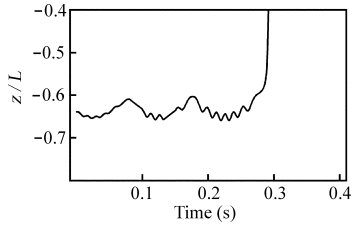

Figure 3. Ganglion's position in the constriction as a function of time obtained from numerical solution of equation 8. $r_{max} = 10^{-4}$ m, $r_{min} = 10^{-5}$ m, $|\nabla P_s| = 1.11 \times 10^6$ N/m^3, $f = 10$ Hz, $a_0 = 28$ m/s^2.

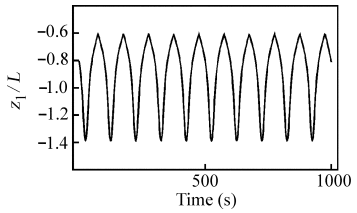

Figure 4. Ganglion's position in the constriction as a function of time. $r_{max} = 10^{-4}$ m, $r_{min} = 10^{-5}$ m, $|\nabla P_s| = 0.55 \times 10^6$ N/m^3, $f = 0.01$ Hz, $a_0 = 591$ m/s^2.

crease in the number of periods are again explained by the interference between the forced and natural oscillations as illustrated by Figure 5. It shows the ganglion's motion for $a_0 = 232$ m/s^2 and $f = 100$ Hz comparable to the natural frequency. As it should be for the superposition of two nearby frequencies, a beating pattern with a complex envelope is observed. The resulting large total amplitude that occurred during the 14th cycle (around 0.15 s) led to the mobilization while a_0 was lower than the predicted value.

The wide pore ($r_{max} = 10^{-3}$ m, $r_{min} = 10^{-4}$ m)

We now turn attention to another extreme case in which both r_{max} and r_{min} have been increased by an order of magnitude. The unplugging-threshold body force, calculated from the maximum capillary-pressure difference, is about 1.143×10^5 N/m^3. The static gradient is set close to it, $|\nabla P_s| = 1.1 \times 10^5$ N/m^3; the predicted mobilizing acceleration $a_0 \approx 4$ m/s^2; the equilibrium configuration is $z_1/L \approx -0.6445$; and the characteristic response time $\tau = 1$ s. Table 2 summarizes the parameters and the results in the same format as in Table 1. For all frequencies (0.01, 0.1, 1 Hz), the predicted mobilizing acceleration is the same as the one calculated from the numerical solution. At all frequencies, the droplet is mobilized during the first cycle of vibrations. Note that for pores of this relatively large diameter ($r_{max} = 1$ mm), only very low frequencies affect the fluids because of the restriction imposed by equation 10.

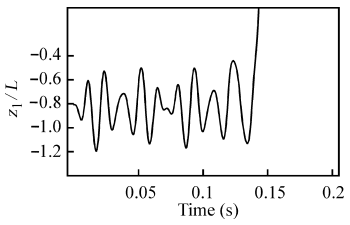

Figure 5. Ganglion's position in the constriction as a function of time. $r_{max} = 10^{-4}$ m, $r_{min} = 10^{-5}$ m, $|\nabla P_s| = 0.55 \times 10^6$ N/m^3, $f = 100$ Hz, $a_0 = 232$ m/s^2.

The smooth pore ($r_{max} = 10^{-3}$ m, $r_{min} = 5 \times 10^{-4}$ m)

The mobilizing accelerations in the previous examples ranged from several to several hundred m/s^2. According to the data available to the author (E. L. Majer, personal communication, 2004; Turpening and Pennington, 2005) and from the author's experience, realistic borehole seismic sources are capable of producing accelerations under the best scenarios not exceeding ~ 0.1 m/s^2 at the distances of a few hundred meters; these accelerations fall off rapidly as the distance increases. These are not significant values. Considering practical applications, should the accelerations be that large as predicted? The following case is instructive because it illustrates an enormous range of accelerations that can lead to oil mobilization in natural porous media, including very low values as well.

This case is different from the previous one in that r_{min} has been brought closer to r_{max}, to make for a smoothly varying pore wall. As a result, the capillary-threshold body force became smaller, $|\nabla P_0| = 11201.452$ N/m^3, and, to illustrate the point, the static gradient is deliberately set to a very close value, $|\nabla P_s| = 11201.45$ N/m^3. The equilibrium configuration is $z_1/L \approx -0.6862$. The predicted mobilizing acceleration is indeed very low, on the order of 2×10^{-6} m/s^2 (Table 3). The values of a_0 obtained from the numerical solution are also given in Table 3; for the frequencies of 0.01 and 0.1 Hz, they are close to the predicted accelerations.

Table 2. Mobilization parameters in the wide ($r_{max} = 10^{-3}$ m, $r_{min} = 10^{-4}$ m) pore. The capillary-threshold body force is 1.143×10^5 N/m^3, $\tau = 1$ s.

External gradient $\lvert\nabla P_s\rvert$ (N/m^3)	Initial condition of ganglion at rest $z_1/L(t = 0)$	Mobilizing acceleration a_0 predicted from the static criterion (m/s^2)	Computed mobilizing acceleration a_0 (m/s^2)			Frequency of breakdown in the static criterion (Hz)
			0.01 Hz	0.1 Hz	1 Hz	
1.1×10^5	−0.6445	4	Between 4–5	Between 4–5	Between 4–5	≈25

Table 3. Mobilization parameters in the smooth ($r_{max} = 10^{-3}$ m, $r_{min} = 5 \times 10^{-4}$ m) pore. The capillary-threshold body force is 11201.452 N/m^3, $\tau = 1$ s.

External gradient $\lvert\nabla P_s\rvert$ (N/m^3)	Initial condition of ganglion at rest $z_1/L(t = 0)$	Mobilizing acceleration a_0 predicted from the static criterion (m/s^2)	Computed mobilizing acceleration a_0 (m/s^2)			Frequency of breakdown in the static criterion (Hz)
			0.01 Hz	0.1 Hz	1 Hz	
11201.45	−0.6862	2×10^{-6}	Between $(1–2) \times 10^{-6}$	Between $(8–9) \times 10^{-7}$ (mobilized after 16 periods)	Between $(1–2) \times 10^{-5}$ (mobilized after 5 periods)	≈0.5

Another notable feature of this simulation is that the estimated frequency of the breakdown in the static mobilization criterion is now about 0.5 Hz. If the forcing frequency is above this value, the mobilizing amplitude must increase, or it will be unable to ensure the necessary transport of the droplet to the neck of the constriction. This point is well illustrated in Table 3 for the forcing frequency of 1 Hz, which is above the critical frequency. The computed mobilizing acceleration at this frequency is an order of magnitude higher than that predicted from the static criterion, as was anticipated.

The numerical solutions for all three combinations of r_{max} and r_{min} allow calculation of an average speed of the ganglion as its right contact line moves to the neck of the constriction. For example, for the case in which $r_{max} = 10^{-4}$ m, $r_{min} = 10^{-5}$ m, the approximate distance $(0.04 \times L)$ separating the right contact line from the neck was traveled in about 0.01 s; this provides the velocity of $\sim 0.04 \times 10^{-2}$ m/0.01 s = 0.04 m/s. On the other hand, the maximum velocity that the fluid would have traveled with, had it not been restricted by the capillary force, can be estimated by the velocity of the Poiseuille flow in the channel with the radius r_{max}, $v_{Pois} = r_{max}^2 |\nabla P_s|/4\mu$ (e.g., Woan, 2002, p. 85). Substituting the mobilizing gradient, $v_{Pois} = (10^{-4}\ \text{m})^2 \times 1.14 \times 10^6\ \text{N/m}^3/(4 \times 10^{-3}\ \text{Pa.s}) \approx 3$ m/s, which is about 75 times faster than the motion controlled by the capillary force alone. Similarly, for the case in which $r_{max} = 10^{-3}$ m and $r_{min} = 10^{-4}$ m, the contact-line velocity is obtained from the travel distance of $\sim 0.04\ L$ and the travel time of ~ 0.04 s (the inverse of the value in the last column of Table 2), to be approximately 0.01 m/s. The corresponding Poiseuille velocity for the mobilizing gradient of 1.14×10^5 N/m^3 is ~ 29 m/s, giving the ratio of 2900. For the case in which $r_{max} = 10^{-3}$ m and $r_{min} = 5 \times 10^{-4}$ m, the contact-line velocity is obtained from the travel distance of $\sim 0.09\ L$ and the traveltime of ~ 2 s (the inverse of the last column of Table 3), to be 5×10^{-4} m/s, and the Poiseuille velocity for the mobilizing gradient of 1.12×10^4 N/m^3 is ~ 3 m/s. The velocity ratio is, therefore, about 6000. Clearly, the viscosity is not a major restricting factor to the motion, compared to the capillary force, which justifies the approximation used in deriving equations 6–8.

CONCLUSIONS AND INFERENCES FOR SEISMIC STIMULATION

This analysis shows that, generally, the accelerations that seismic sources need to develop to overcome the capillary barrier in realistic pore structures are on the order of at least several m/s^2 or even much higher. We have already observed that realistic borehole sources produce the accelerations about 0.1 m/s^2 measured at the distances of a few hundred meters; this may be insufficient to stimulate significant volumes of the reservoirs. Much larger accelerations can be created, however, by surface shakers that can be used to stimulate the movement of entrapped fluids in the shallow environment, arising, for example, from groundwater contamination by organic pollutants.

On the other hand, this necessary acceleration level can also be extremely low, depending on how close a particular ganglion resides to its mobilization threshold; in other words, how wide is the gap between $|\nabla P_s|$ and $|\nabla P_0|$ in our previous discussion. Ganglia entrapped very near their unplugging thresholds (having narrow gaps) may only need a slight extra push to become liberated; such forcing may be provided even by ambient vibrations. In a natural porous medium, the thresholds will be highly variable, depending on a particular pore's geometry, the wetting angle, and the surface tension between the phases. Owing to a vastly irregular character of the reservoir porous space, these thresholds are hardly predictable. Therefore, it would be a nonfeasible task to forecast the volume of oil released by the application of vibrations of a particular amplitude and frequency in a natural rock, not because the process is poorly understood (for any particular geometry, the effect can be calculated) but because the character of the porous space is unknown. This task would only be possible if some average characteristics of pore openings and throats, as well as the contact angles, are firmly established. The roughness of pore walls contributes to the uncertainty.

It is clear, though, that vibrations of any amplitude and frequency will always produce a certain mobilization effect, as they will unplug the ganglia for which the mobilization conditions are satisfied, leaving others intact. As our examples show, there will always be a subset of ganglia in the entrapped population that lie close enough to the unplugging threshold to be liberated by any vibration, however small the amplitude. Experiments in deep and shallow natural environments are needed in addition to this theory to establish the payoff of using elastic waves and vibrations as a tool for enhanced petroleum recovery.

ACKNOWLEDGMENTS

This work was partially supported by the National Science Foundation. The author is grateful to Pavel Iassonov, Wenqing Li, Dennis Vigil, and Robert Ewing for stimulating discussions in the course of this study. Comments by the associate editor and three anonymous reviewers are highly appreciated.

APPENDIX A

REPRESENTATION OF THE VIBRATION-INDUCED BODY FORCE

In a channel experiencing a vibration of the wall, the inertial body force acting on the fluid is obtained by rewriting the equation of motion of the fluid in the frame of reference of the wall. For the fluid velocity $\mathbf{V}$ and the wall moving along the z-axis with the velocity $v(t)$, the axial and radial components of the fluid velocity $\mathbf{v}_1$ relative to the wall are $v_{1z} = V_z - v(t)$ and $v_{1r} = V_r$. The incompressible Navier-Stokes equation is

$$\rho_f \frac{\partial \mathbf{V}}{\partial t} + \rho_f (\mathbf{V}\nabla)\mathbf{V} = -\ \nabla P + \mu \nabla^2 \mathbf{V}, \qquad \text{(A-1)}$$

where μ is the fluid viscosity and ∇^2 is the Laplacian (e.g., Landau and Lifshitz, 1975, equation 15.7).

The axial component of equation A-1 is

$$\rho_f \frac{\partial V_z}{\partial t} + \rho_f \left(V_r \frac{\partial V_z}{\partial r} + V_z \frac{\partial V_z}{\partial z} \right) = -\frac{\partial P}{\partial z} + \mu \left[\frac{1}{r} \frac{\partial}{\partial r} \left(r \frac{\partial V_z}{\partial r} \right) + \frac{\partial^2 V_z}{\partial z^2} \right] \qquad \text{(A-2)}$$

(Landau and Lifshitz, 1975, equations 15.16), where the axial symmetry (velocity independence of the azimuthal angle) has been taken into account. Substituting $V_z = v_{1z} + v(t)$ and $V_r = v_{1r}$ into equation A-2, we obtain

$$\rho_f \frac{\partial}{\partial t}[v_{1z} + v(t)] + \rho_f \left\{ v_{1r} \frac{\partial}{\partial r}[v_{1z} + v(t)] + [v_{1z} + v(t)] \right.$$

$$\times\frac{\partial}{\partial z}[v_{1z}+v(t)]\Bigg\}$$
$$=-\frac{\partial P}{\partial z}+\mu\Bigg\{\frac{1}{r}\frac{\partial}{\partial r}\Bigg\{r\frac{\partial}{\partial r}[v_{1z}+v(t)]\Bigg\}$$
$$+\frac{\partial^2}{\partial z^2}[v_{1z}+v(t)]\Bigg\}, \qquad \text{(A-3)}$$

which considering that $v(t)$ is independent of r and z, and that $a(t) = \partial v(t)/\partial t$, simplifies to

$$\rho_f\frac{\partial v_{1z}}{\partial t}+\rho_f\left(v_{1r}\frac{\partial v_{1z}}{\partial r}+v_{1z}\frac{\partial v_{1z}}{\partial z}\right)$$
$$=-\frac{\partial P}{\partial z}+\mu\left[\frac{1}{r}\frac{\partial}{\partial r}\left(r\frac{\partial v_{1z}}{\partial r}\right)+\frac{\partial^2 v_{1z}}{\partial z^2}\right]$$
$$-\rho_f\left[a(t)+v(t)\frac{\partial v_{1z}}{\partial z}\right]. \qquad \text{(A-4)}$$

We now notice that equation A-4 is the same as equation A-2 with the only difference in the appearance of the additional body-force term

$$S_z \equiv -\rho_f\left[a(t)+v(t)\frac{\partial v_{1z}}{\partial z}\right] \qquad \text{(A-5)}$$

(in its right-hand side) that is responsible for the effect of the vibrating wall. This means that a switch to the frame of reference of the moving wall is equivalent to the addition of an inertial body force with the axial component S_z.

Similarly, substituting $V_z = v_{1z} + v(t)$, and $V_r = v_{1r}$ into the radial component of equation A-1 (Landau and Lifshitz, 1975, equations 15.16) leads us to the equation for v_{1r}, from which the radial component of the external body force is

$$S_r \equiv -\rho_f v(t)\frac{\partial v_{1r}}{\partial z}. \qquad \text{(A-6)}$$

As seen from equations A-5 and A-6, the additional source terms acting on the fluid reduce to approximately $S_z = -\rho_f a(t)$ if the z-derivatives of the fluid velocity vanish. For the fluid in a sinusoidally constricted channel, these derivatives are of approximately the same absolute value but opposite sign on the two sides of the constriction; thus, they will approximately cancel each other in the total body forces S_z and S_r acting on the fluid. This justifies using the representation $-\rho_o a(t)$ for the oscillatory body force in our model.

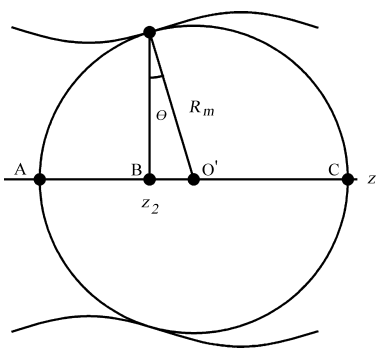

Figure B-1. Geometry of the spherical caps.

APPENDIX B

CALCULATION OF THE CENTER OF MASS OF THE GANGLION

The coordinate of the center of mass of the ganglion z_c is

$$z_c = \frac{1}{V_g}\int\int_{V_g}\int zrdrdzd\varphi, \qquad \text{(B-1)}$$

where V_g is the ganglion's volume,

$$V_g = \int\int_{V_g}\int rdrdzd\varphi \qquad \text{(B-2)}$$

(e.g., Harris and Stocker, 1998, p. 583).

The volume integrals B-1 and B-2 can be conveniently calculated in three steps: over the body of the ganglion limited by the vertical planes containing the contact lines z_1 = const and z_2 = const (Integral I), over the right spherical cap (Integral II), and over the left spherical cap (Integral III) (Figure 2). Integral I for equation B-1 becomes $\mathrm{I}_{(\text{B-1})} \equiv \int_{z_1}^{z_2}\int_0^{r(z)}\int_0^{2\pi} zrdzdrd\varphi$, which, taking equation 3 into account and after straightforward but tedious manipulations, evaluates to

$$\mathrm{I}_{(\text{B-1})} = \pi r_{\max}^2\left\{\begin{array}{l}\frac{z_2^2-z_1^2}{2}\frac{r_{\min}}{r_{\max}}\left[1+\frac{3}{8}\frac{r_{\min}}{r_{\max}}\left(1-\frac{r_{\max}}{r_{\min}}\right)^2\right]\\ +\frac{1}{2}\frac{L}{\pi}\left(\frac{r_{\min}^2}{r_{\max}^2}-1\right)\left[\frac{L}{\pi}\left(\cos\pi\frac{z_2}{L}-\cos\pi\frac{z_1}{L}\right)+\left(z_2\sin\pi\frac{z_2}{L}-z_1\sin\pi\frac{z_1}{L}\right)\right]\\ +\frac{1}{16}\frac{L}{\pi}\left(\frac{r_{\min}}{r_{\max}}-1\right)^2\left[\frac{1}{2}\frac{L}{\pi}\left(\cos 2\pi\frac{z_2}{L}-\cos 2\pi\frac{z_1}{L}\right)+\left(z_2\sin 2\pi\frac{z_2}{L}-z_1\sin 2\pi\frac{z_1}{L}\right)\right]\end{array}\right\}. \qquad \text{(B-3)}$$

To calculate Integral II for equation B-1, the equation of the spherical cap should be written. This can be done with the help of Figure B-1, where O′ stands for the center of the sphere, of which the right meniscus is the spherical segment to the right of the contact line, and $\tan\theta = r'(z_2)$. The same equation will hold for the left meniscus, with the difference that the latter will constitute the spherical segment to the left of the contact line, with z_2 replaced with z_1.

From Figure B-1 and equation 4, the equation of the sphere is $z'^2 + r^2 = R_m^2(z_2) = r^2(z_2)[1 + r'^2(z_2)]$, where the axial coordinate z' is counted from the sphere center O'. Considering that $z' = z - z_2 - \mathrm{BO}'$ and $\mathrm{BO}' = r(z_2)r'(z_2)$, the sphere's equation becomes $r = \sqrt{r^2(z_2)[1 + r'^2(z_2)] - [z - z_2 - r(z_2)r'(z_2)]^2}$. The right meniscus is the segment of the sphere limited by z changing from z_2 to $z_R \equiv z_2 + \mathrm{BC} = z_2 + \mathrm{BO}' + R_m(z_2) = z_2 + r(z_2)[r'(z_2) + \sqrt{1 + r'^2(z_2)}]$ (Figure B-1), where z_R is the right (upper) limit corresponding to point C. The integral over the right spherical cap becomes $\mathrm{II}_{(\text{B-1})} = 2\pi\int_{z_2}^{z_R}\int_0^{\sqrt{r^2(z_2)[1+r'^2(z_2)]-[z\,-\,z_2\,-\,r(z_2)r'(z_2)]^2}} zrdzdr$, which, after intermediate manipulations, equates to

$$\mathrm{II}_{(\mathrm{B\text{-}1})} = \frac{\pi}{2}\{r^2(z_2)[1 + r'^2(z_2)] - [z_2 + r(z_2)r'(z_2)]^2\}(z_R^2 - z_2^2) + \frac{2\pi}{3}[z_2 + r(z_2)r'(z_2)](z_R^3 - z_2^3) - \frac{\pi}{4}(z_R^4 - z_2^4), \tag{B-4}$$

where $r(z_2)$ is again defined by equation 3.

Similarly, the left meniscus is the segment of the sphere limited by z changing from $z_L \equiv z_1 - \mathrm{AB} = z_1 - [R_m(z_1) - \mathrm{BO}'] = z_1 - r(z_1) \times [-r'(z_1) + \sqrt{1 + r'^2(z_1)}]$ to z_1 (Figure B-1, where z_2 has been replaced with z_1), where z_L is the left (lower) limit corresponding to point A. The integral over the left spherical cap thus is $\mathrm{III}_{(\mathrm{B\text{-}1})} = 2\pi\int_{z_L}^{z_1}\int_0^{\sqrt{r^2(z_1)[1+r'^2(z_1)]-[z - z_1 - r(z_1)r'(z_1)]^2}} zrdzdr$, evaluating to

$$\mathrm{III}_{(\mathrm{B\text{-}1})} = \frac{\pi}{2}\{r^2(z_1)[1 + r'^2(z_1)] - [z_1 + r(z_1)r'(z_1)]^2\}(z_1^2 - z_L^2) + \frac{2\pi}{3}[z_1 + r(z_1)r'(z_1)](z_1^3 - z_L^3) - \frac{\pi}{4}(z_1^4 - z_L^4). \tag{B-5}$$

The volume integral in equation B-1 is the sum of $\mathrm{I}_{(\mathrm{B\text{-}1})} + \mathrm{II}_{(\mathrm{B\text{-}1})} + \mathrm{III}_{(\mathrm{B\text{-}1})}$ (equations B-3–B-5).

The calculation of the volume of the blob B-2 is performed in exactly the same manner as the sum of the integrals over the oil body between z_1 and z_2 (Integral I) and over the right and the left spherical caps (Integrals II and III, respectively). The integration gives

$$\mathrm{I}_{(\mathrm{B\text{-}2})} = \pi r_{\max}^2 \left\{ \begin{array}{l} \dfrac{r_{\min}}{r_{\max}}\left[1 + \dfrac{3}{8}\dfrac{r_{\min}}{r_{\max}}\left(1 - \dfrac{r_{\max}}{r_{\min}}\right)^2\right](z_2 - z_1) \\ + \dfrac{1}{2}\dfrac{L}{\pi}\left(\dfrac{r_{\min}^2}{r_{\max}^2} - 1\right)\left(\sin\pi\dfrac{z_2}{L} - \sin\pi\dfrac{z_1}{L}\right) \\ + \dfrac{1}{16}\dfrac{L}{\pi}\left(\dfrac{r_{\min}}{r_{\max}} - 1\right)^2\left(\sin 2\pi\dfrac{z_2}{L} - \sin 2\pi\dfrac{z_1}{L}\right) \end{array} \right\}, \tag{B-6}$$

$$\mathrm{II}_{(\mathrm{B\text{-}2})} = \pi\{r^2(z_2)[1 + r'^2(z_2)] - [z_2 + r(z_2)r'(z_2)]^2\}(z_R - z_2) + \pi[z_2 + r(z_2)r'(z_2)](z_R^2 - z_2^2) - \frac{\pi}{3}(z_R^3 - z_2^3), \tag{B-7}$$

$$\mathrm{III}_{(\mathrm{B\text{-}2})} = \pi\{r^2(z_1)[1 + r'^2(z_1)] - [z_1 + r(z_1)r'(z_1)]^2\}(z_1 - z_L) + \pi[z_1 + r(z_1)r'(z_1)](z_1^2 - z_L^2) - \frac{\pi}{3}(z_1^3 - z_L^3). \tag{B-8}$$

The ganglion's total volume is $V_g = \mathrm{I}_{(\mathrm{B\text{-}2})} + \mathrm{II}_{(\mathrm{B\text{-}2})} + \mathrm{III}_{(\mathrm{B\text{-}2})}$ (equations B-6–B-8).

It is not difficult to check that, in the limiting case of a cylindrical capillary [$r_{\min} = r_{\max} \equiv R_c$, $r'(z) = 0$], the total volume reduces to the correct value of $\pi R_c^2\left(z_2 - z_1 + \frac{4}{3}R_c\right)$ and the center of mass z_c, calculated using equations B-1–B-8, lies in the middle of the blob, $z_c = (z_1 + z_2)/2$, as it should.

APPENDIX C

VARIABILITY IN THE LENGTH AND COORDINATE OF THE CENTER-OF-MASS OF THE GANGLION

To get insight into how variations in the length of the ganglion, as it moves toward the neck of the constriction, affect the results obtained in the constant-length approximation, we chose the worst-scenario case of the largest capillary threshold and with the ganglion away from the constriction, that is, corresponding to $r_{\max} = 10^{-4}$ m, $r_{\min} = 10^{-5}$ m, Case 2.

To illustrate the full range of variability, the ganglion's volume is chosen in such a way that $l/L = (z_2 - z_1)/L = 0.6$ is exactly at $z_1/L = -1$ (Figure 2); this volume was calculated from equations B-6–B-8 for the given z_1 and z_2, $V_g = 1.2244 \times 10^{-10}$ m^3. Then, for a series of the left-contact-line positions z_1/L and this constant volume, the coordinate z_2/L was calculated as the root of the algebraic equation $V_g(z_1, z_2) = 1.2244 \times 10^{-10}$ m^3; l then is simply $z_2 - z_1$. The resulting dependence of the ganglion's length on z_1/L is depicted in Figure C-1.

It can be seen (considering the initial length of the ganglion $l/L = 0.6$) that the length rises quickly as the blob enters the constriction (the beginning part of the plot in Figure C-1). The implications for our simulation is that the ganglion, whose initial configuration is $z_1/L = -0.8070$ (Table 1, second row), will quickly increase in length to $l/L \approx 0.8$ and become mobilized. Its actual length between the start of the motion and the mobilization moment will be between 0.6 L and 0.8 L. Thus, one should see how this increase in the effective length will affect the conclusions of the analysis.

The maximum capillary-pressure difference across the length of the ganglion for $l = 0.8\,L$ is ~7125 Pa, from which the unplugging-threshold body force is 7125 Pa/$(0.8 \times 10^{-2}$ m$) \approx 0.891 \times 10^6$ N/m^3. The predicted mobilizing acceleration for the static gradient of 0.55×10^6 N/m^3 is then ~341 m/s^2 (cf. 591 m/s^2 for $l = 0.6\,L$, Table 1). For the new length, the frequency of breakdown in the static criterion decreases to ~30 Hz (cf. 200 Hz for $l = 0.6\,L$). The realistic values of these quantities for a ganglion with variable length can thus be expected to lie somewhere between these extremes.

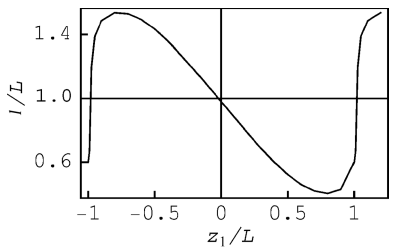

Figure C-1. Ganglion's length as a function of the position of the left contact line in the pore. $r_{\max} = 10^{-4}$ m, $r_{\min} = 10^{-5}$ m, $V_g = 1.2244 \times 10^{-10}$ m^3.

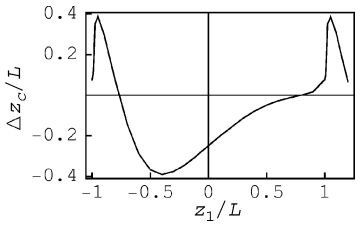

Figure C-2. Uncertainty in the center-of-mass calculation: $r_{max} = 10^{-4}$ m, $r_{min} = 10^{-5}$ m, $V_g = 1.2244 \times 10^{-10}$ m^3.

We now estimate how the assumption of the fixed center-of-mass affects the results. To that end, we calculate the difference between the assumed fixed position of the center-of-mass and its actual position $z_c(z_1,z_2)$ calculated from equations B-1–B-8: $\Delta z_c \equiv (z_1 + z_2)/2 - z_c(z_1,z_2)$. The calculation is performed for the same z_1, z_2 pairs that were used to construct Figure C-1. The result is depicted in Figure C-2 as a function of the left-contact-line position z_1/L. The leftmost positive part of the curve is of interest to this analysis, because it corresponds to the ganglion still to the left of the constriction until it is liberated ($\Delta z_c/L > 0$: the real center-of-mass is behind because it is shifted to the left by the thick body of the ganglion occupying the open part of the pore). An average uncertainty of about 0.2 L in the location of the ganglion is expected, amounting to about 0.2 L/0.6$L \approx 30\%$ of the blob's length.

REFERENCES

Averbakh, V. S., S. N. Vlasov, and Y. M. Zaslavsky, 2000, Motion of a liquid droplet in a capillary under the action of static force and an acoustic field: Radiophysics and Quantum Electronics, **43**, 142–147.

Beresnev, I. A., and P. A. Johnson, 1994, Elastic-wave stimulation of oil production: A review of methods and results: Geophysics, **59**, 1000–1017.

Beresnev, I. A., R. D. Vigil, W. Li, W. D. Pennington, R. M. Turpening, P. P. Iassonov, and R. P. Ewing, 2005, Elastic waves push organic fluids from reservoir rock: Geophysical Research Letters, **32**, L13303.

Biot, M. A., 1956, Theory of propagation of elastic waves in a fluid-saturated porous solid. II. Higher frequency range: Journal of the Acoustical Society of America, **28**, 179–191.

Graham, D. R., and J. J. L. Higdon, 2000, Oscillatory flow of droplets in capillary tubes. Part 2. Constricted tubes: Journal of Fluid Mechanics, **425**, 55–77.

Harris, J. W., and H. Stocker, 1998, Handbook of mathematics and computational science: Springer Publishing Company, Inc.

Hilpert, M., G. H. Jirka, and E. J. Plate, 2000, Capillarity-induced resonance of oil blobs in capillary tubes and porous media: Geophysics, **65**, 874–883.

Iassonov, P. P., and I. A. Beresnev, 2003, A model for enhanced fluid percolation in porous media by application of low-frequency elastic waves: Journal of Geophysical Research, **108**, ESE 2-1–2-9.

Johnson, R. W., 1998, The handbook of fluid dynamics: CRC Press.

Landau, L. D., and E. M. Lifshitz, 1975, Fluid mechanics: Pergamon Press, Inc.

Li, W., R. D. Vigil, I. A. Beresnev, P. P. Iassonov, and R. P. Ewing, 2005, Vibration-induced mobilization of trapped oil ganglia in porous media: Experimental validation of a capillary-physics mechanism: Journal of Colloid and Interface Science, **289**, 193–199.

Melrose, J. C., and C. F. Brandner, 1974, Role of capillary forces in determining microscopic displacement efficiency for oil recovery by waterflooding: The Journal of Canadian Petroleum Technology, October-December, 54–62.

Nikolaevskiy, V. N., G. P. Lopukhov, Y. Liao, and M. J. Economides, 1996, Residual oil reservoir recovery with seismic vibrations: SPE Production and Facilities, May, 89–94.

Poesio, P., G. Ooms, S. Barake, and F. van der Bas, 2002, An investigation of the influence of acoustic waves on the liquid flow through a porous material: Journal of the Acoustical Society of America, **111**, 2019–2025.

Roberts, P. M., 2005, Laboratory observations of altered porous fluid flow behavior in Berea sandstone induced by low-frequency dynamic stress simulation: Acoustical Physics, **51**, S140–S148.

Roberts, P. M., I. B. Esipov, and E. L. Majer, 2003, Elastic wave stimulation of oil reservoirs: Promising EOR technology?: The Leading Edge, **22**, 448–453.

Roberts, P. M., A. Sharma, V. Uddameri, M. Monagle, D. E. Dale, and L. K. Steck, 2001, Enhanced DNAPL transport in a sand core during dynamic stress stimulation: Environmental Engineering Science, **18**, 67–79.

Turpening, R. M., and W. D. Pennington, 2005, Calibration and testing of sonic stimulation technologies: U. S. Department of Energy, Final Report DE-FC26-01BC15165, http://www.geo.mtu.edu/spot/Calibration_Sonic/FinalReportMTU_BC15165.pdf, accessed May, 5, 2006.

Woan, G., 2002, The Cambridge handbook of physics formulas: Cambridge Univ. Press.